Grain Size, Misorientation, and Texture Evolution of Copper Processed by Equal Channel Angular Extrusion and the Validity of the Hall–Petch Relationship

FLORIAN H. DALLA TORRE, AZDIAR A. GAZDER, CHENG F. GU, CHRISTOPHER H.J. DAVIES, and ELENA V. PERELOMA

The microstructure and texture of copper subjected to equal channel angular extrusion (ECAE) *via* route B_C for up to 16 passes have been assessed using electron backscatter diffraction (EBSD), transmission electron microscopy (TEM), X-ray diffraction (XRD) peak broadening, and texture analysis. The differences in grain size measured by these techniques allows for an understanding of microstructural evolution. A gradual decrease in grain size occurs with an increasing number of passes, while the subgrain size remains approximately constant. Up to four passes, the fraction of high-angle grain boundaries (HAGBs) (> 15 deg) increases from 15 to 45 pct, but remains constant thereafter. The grain boundary character distribution shows a decrease of $\Sigma 1$ boundaries and an increase of $\Sigma 3$ boundaries with higher passes. After 16 passes, a few regions of large 1 to 4 μm sized grains embedded in a submicrometer sized matrix were observed. These agglomerates of larger grain diameters together with the measured decrease in the dislocation density correlate with the observed decrease in yield strength of samples subjected to four and more passes. Texture evolution is adequately described under conditions of negative simple shear. The effect of increased accumulated strain results in an overall spread of orientation densities due to the absence of stable end positions post-ECAE. Detailed microstructural information suggests that strengthening mechanisms in the material can be sufficiently well described by the classical Hall–Petch relationship by applying it to the subgrain size, while the subgrain size remains smaller than the grain size.

DOI: 10.1007/s11661-007-9103-z

I. INTRODUCTION

WHEN the average crystal size of a material is smaller than 1 μm, methods involving electron microscopy or X-ray diffraction (XRD) are used to quantify grain size. Although these techniques do not necessarily return the same results, they complement each other and enable a better understanding of microstructural peculiarities. Using a high resolution (HR) scanning electron microscope (SEM) equipped with a field emission gun (FEG) and newly developed automated processes for electron backscatter diffraction (EBSD), large area scans are possible for materials having grain sizes lower than 500 nm. Compared to transmission electron microscopy (TEM), EBSD returns significantly improved microstructural statistics. Consequently, the latter technique has been successfully applied to heavily deformed metals with grain sizes less than a micrometer.[1,2]

Below 100 nm, grain size indexing becomes difficult using EBSD. Thus, XRD peak broadening analysis is favored where high statistical grain size measurements are deduced from scans on areas several square millimeters in size. This is often coupled with direct grain size measurements by TEM. The combination of TEM and X-ray techniques yields a clearer interpretation of the coherently scattered domains.[3] Furthermore, the advantage of TEM lies in its capability to reveal misorientation relationships *via* tilting experiments in microdiffraction. Although such experiments have been used to characterize heavily deformed metals,[4,5] they are also tedious and time consuming.

In a fine-grained material with a homogeneous microstructure composed of random high-angle grain boundaries (HAGBs), grain size comparisons obtained by EBSD and TEM or XRD peak broadening analysis have shown close agreement.[1,6] However, in a material subjected to equal channel angular extrusion (ECAE), the microstructure is often inhomogeneous and consists not only of grains confined by HAGBs, but is also characterized by different dislocation substructures. These microstructural variations can therefore provide different sizes depending on the technique and taxonomy

FLORIAN H. DALLA TORRE, Postdoctor, is with the Department of Materials Engineering, Monash University, Victoria 3800, Australia. and the Laboratory of Metal Physics and Technology, Department of Materials, ETH Zurich, 8093 Zurich, Switzerland. Contact e-mail: florian.dallatorre@mat.ethz.ch AZDIAR A. GAZDER, PhD Student, CHENG F. GU, Research Assistant, CHRISTOPHER H.J. DAVIES, Associate Professor, is with the Department of Materials Engineering, Monash University, and the Victorian Centre for Advanced Materials Manufacturing, Victoria, Australia and ELENA V. PERELOMA, Professor, is with the Department of Materials Engineering, Monash University, the Victorian Centre for Advanced Materials Manufacturing, Victoria, and with the BlueScope Steel Metallurgy Centre, School of Mechanical, Materials and Mechatronics Engineering, Faculty of Engineering, University of Wollongong, Wollongong, Australia.

Manuscript submitted February 24, 2006.
Article published online May 12, 2007.

used to classify the microstructure. This is illustrated by comparing the definitions of a "cell" or "grain" in taxonomies based on EBSD, TEM, and XRD.[1,6,7]

The nomenclature proposed by Hughes *et al.*[8] based on TEM observations has achieved widespread acceptance and divides the microstructure into a well-defined hierarchy. Therein, cells are described as roughly equiaxed volumes where the dislocation density is well below the average and which are bounded by low-angle dislocation boundaries. Often found in unidirectional deformation, lamellar boundaries (LBs) are characterized by their straight and parallel structure, are built up by dense dislocation walls (DDWs), and separate volumes of higher misorientation due to the operation of different glide systems.[8] More than two such closely spaced LBs are defined as microbands. Subgrains are defined as dislocation-free volumes surrounded by medium- to high-angle boundaries. In a recent TEM study on ECAE-processed aluminum,[4] a correlation was found between the phenomenological appearance of a boundary or wall and its misorientation. Irrespective of the accumulated strain, sharp grain boundaries (GBs) had misorientations larger than 15 deg, while polygonized dislocation walls (PDWs), which show densely spaced dislocations (unlike DDWs), exhibited misorientation angles of 1 to 5 deg.

In contrast to these observations, XRD peak broadening analysis has led to a description of the microstructure[9,10,11] based on the coherent scattering of domains. Because no coherency results from X-rays scattered from different cells, the microstructural features with the shortest average spacing between misorientations are measured. Therefore, in a nanograined material consisting only of HAGBs, the measured coherent domain size is equal to the grain size.[6] Alternatively, the measurement would correspond to the cell size if the spacing of the cell walls is less than that of the HAGBs. High-resolution XRD *via* synchrotron radiation allows for a further distinction between cells, which with increasing deformation reflects a transformation of cell walls with a Burgers vector parallel to the cell walls (polarized dipole wall) to cell walls with perpendicular Burgers vectors (polarized tilt wall) and, thus, qualitatively yields an estimate of the degree of misorientation of cells.[11]

A more straightforward definition of the microstructural features is derived by EBSD measurements. There, grains and subgrains can be differentiated using their misorientation angle, which is >15 deg (or HAGBs) and <15 deg (or low-angle grain boundaries (LAGBs)), respectively. However, at very low angles (2 to 3 deg), a differentiation of misorientation indices is not detectable any more and this therefore represents the lower angular limit for the identification of single cells.

In order to predict mechanical properties of heavily deformed microstructures, accurate knowledge of the different microstructural features, misorientation relationships, and the type of obstacles accumulated in the deformed microstructure is required. For example, it has been pointed out[12] that the Hall–Petch (H-P) relationship (which predicts flow stress dependency on the reciprocal square root of the grain size[13,14]) holds for undeformed polycrystalline metals down to a grain size of below 100 nm.[15,16,17] However, a deviation of this H-P relationship occurs in heavily deformed metals due to different strengthening mechanisms at high- and low-angle GBs.[18,19] Li *et al.*[20] explained the transition from hardening to softening in ultra-fine-grained (UFG) copper (Cu) on the basis of a differentiation between subgrain and grain sizes. They assumed that mechanical properties are controlled solely by the subgrain diameter (comprising LAGBs) only if it is comparatively smaller than the grain diameter (which consists of HAGBs). If, however, these diameters are approximately equal, the mechanical properties are controlled by the grain size, which in turn shows a different ability to store and annihilate lattice dislocations. Using this concept, Li *et al.*[20]. explained the temperature influence on the flow stress of Cu specimens deformed to various degrees of strain.

In the following sections, TEM, XRD, and EBSD have been applied to Cu subjected to ECAE *via* route*

*In multipass ECAE, the four processing "routes" are designated by rotating the billet clockwise (CW) or counterclockwise (CCW) through a defined angle (when viewed from the top of the entry channel) around its longitudinal axis before reinsertion for the next pass. They are as follows: routes A (0 deg), B_A (± 90 deg), B_C (90 deg), and C (180 deg), respectively.

B_C processing for $N = 1$, 4, 8, 12, and 16. The ECAE was invented and introduced by Segal *et al.*[21] and is a widely used severe plastic deformation (SPD) technique capable of producing bulk samples with UFG microstructures. Under ideal conditions, the deformation during ECAE processing is restricted to the die channel intersection area and results in the formation of simple shear (SS) type texture components. This study builds on previous work on equal channel angular extruded Cu[22] by (1) presenting a comprehensive picture of microstructural evolution, (2) providing quantitative distributions of grain and subgrain sizes and misorientation relationships, and (3) discussing the development of bulk texture. This information is applied to the classical H-P equation and compared to a recently suggested alternative H-P relationship given in Reference 12. The comparative changes in misorientation, grain size, and subgrain sizes with greater accumulated strain provide a clearer understanding of their influence on strengthening effects in UFG metals.

II. EXPERIMENTAL DETAILS

A commercially sourced Cu rod (99.95 pct purity) was cut into billets of $20 \times 20 \times 80$ mm^3 and annealed at 873 K for 2 hours in an inert atmosphere. This typically results in an equiaxed grain structure with a large fraction of random HAGBs. The distribution of grain size in the annealed material measured using optical microscopy was best fitted by a lognormal distribution function with a peak grain size of 10 μm and a peak width of 0.6 μm. A value of 21 ± 16 μm was measured for the mean grain size (Table I).

Three die inserts were arranged to form an L-shaped channel within the ECAE die cradle (Figure 1). Subse-

Table I. Measurements of Various Microstructural Features for Copper after $N = 0$, 1, 4, 8, 12, and 16 Passes

Microstructural Properties	Number of Passes					
	$N = 0$	$N = 1$	$N = 4$	$N = 8$	$N = 12$	$N = 16$
Mean grain size (μm) (optical microscopy)	21 ± 16	NA	NA	NA	NA	NA
EBSD						
Step size 80 nm						
mean ECD grain size (nm)	NA	1200 ± 2000	640 ± 550	580 ± 400	570 ± 400	570 ± 350
grain AR	NA	3.0 ± 2.5	1.1 ± 1.1	1.1 ± 1.1	1.1 ± 1.4	1.2 ± 1.5
mean ECD subgrain size (nm)	NA	230 ± 150	270 ± 160	270 ± 200	230 ± 130	240 ± 200
AR	NA	1.15 ± 1.4	1.0 ± 1.3	1.05 ± 1.2	1.05 ± 1.4	1.05 ± 1.2
Step size 40 nm						
mean ECD grain size (nm)	NA	NA	190 ± 120	220 ± 180	230 ± 210	170 ± 250
AR	NA	NA	1.36 ± 1.6	0.97 ± 1.2	1.04 ± 1.36	NA
mean ECD subgrain size (nm)	NA	NA	120 ± 60	120 ± 80	130 ± 80	120 ± 100
AR	NA	NA	1.17 ± 1.4	0.93 ± 1.2	0.99 ± 1.33	NA
LAGB intercept (nm)	NA	NA	230	180	190	180
volume fraction HAGB (pct)	NA	15 ± 5	45 ± 10	48 ± 10	45 ± 7	45 ± 5
number of LAGB/number of HAGB	NA	3.81	1.83	1.14	1.26	1.24
pct of total CSL boundaries Σ1	NA	75.83	61.7	51.1	53.5	52.9
pct of total CSL boundaries Σ3	NA	1.5	2.1	2.5	3.4	3.1
pct of random boundaries Σ1	NA	33.8	27.1	22.6	23.8	23.3
pct of random boundaries Σ3	NA	0.7	1.2	1.4	1.9	1.8
TEM[1]						
microband spacing (nm)	NA	400 ± 250	220 ± 130	290 ± 160	NA	NA
subgrain/cell sizes (nm)	NA	220 ± 300	170 ± 130	170 ± 120	165 ± 90	170 ± 80
subgrain/cell wall thickness (nm)	NA	52 ± 48	48 ± 31	37 ± 35	23 ± 8	34 ± 14
number of sharp GBs (per 10 μm^2)	NA	0	13	14	63	80
XRD[1]						
mean FWM {111} (deg)	0.11[2]	0.164	0.190	0.177	0.165	0.144
mean FWM {200} (deg)	0.10[2]	0.343	0.330	0.301	0.231	0.213
coherent domain size (nm)	NA	60	58	57	62	71
lattice strain (pct)	NA	0.05	0.07	0.05	0.03	0.03

[1]Partially, some of the TEM and XRD results have been previously presented (Ref. [22]).
[2]Note that, due to the additional instrumental broadening and surface damage effects, these values represent the upper limit.

quently, room temperature (RT) $\Phi = 90$ deg, $\Psi = 0$ deg ECAE processing *via* route B_C was conducted with a back-pressure of 60 MPa and a forward speed of 2 mm s^{-1}, resulting in an equivalent strain of ~1.15 per pass.[23] In order to reduce friction, the die channels and billets were lubricated with a coating of graphite film and MoS_2 mineral oil. The billets were subjected to 1, 2, 4, 8, 12, and 16 passes (N). Between successive passes, the billets were ground back to their original dimensions using a water soluble oil (40:1 water/oil ratio), which served as both lubricant and cooling medium. Billets and specimens were stored at RT between extrusions and before and during microstructural analysis, respectively.** Figure 1 describes the adopted coordinate system as a schematic of a billet undergoing ECAE with the extrusion direction (ED), normal direction (ND), and transverse direction (TD) corresponding to the laboratory xyz axes, respectively. As suggested previously, the billet undergoes deformation *via* negative SS on the $\acute{y}$ plane in the $\acute{x}$ direction at the intersection of the entry and exit channels.

Specimen sections cut from the center of the stable billet length and perpendicular to the ED were used for microstructural characterization by TEM, XRD, and EBSD. Hereafter, they will also be referred to as the ED samples. The backscatter measurements were performed at the center of the cross section of the $20 \times 20 \times 3$ mm^3 samples using a LEO-1530 FEG-SEM fitted with a NORDLYS-II† EBSD detector. Mostly, a scan area of 10×18 μm^2 with a 40- or 80-nm step size was used in the center of specimen. In specific cases, larger scans of up to 30×40 μm^2 were also performed. Postprocessing of the raw data was undertaken using VMAP[1] and

**It should be noted that due to SPD, recovery processes might be active within the material. Generally, the rate of recovery follows an Arrhenius-type time dependence. Consequently, the billet will experience the highest rates of recovery upon immediate release of hydrostatic pressure conditions during its removal from the ECAE die due to vacancy diffusion. Recovery during grinding or sample section preparation for TEM, EBSD, and texture analyses will continue, but at vastly slower rates. Again, recovery effects from storage at RT are believed to occur but to comparably smaller amounts.

†NORDLYS-II is a trademark of HKL Technology, Hobro, Denmark (now Oxford Instruments Group).

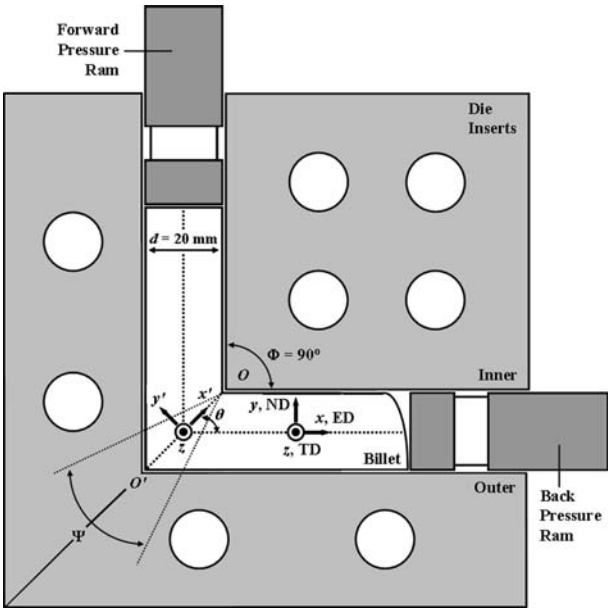

Fig. 1—Schematic drawing of the ECAE billet and the adopted convention used for describing billet coordinates.

HKL-Channel 5[‡]. For grain and subgrain size measurements, the equivalent circle diameter (ECD) method is used, wherein the area is measured and the grain/subgrain size is defined as the diameter of a circle with area the same as the measured area of the grain. In the 256-color EBSD maps, the various colors represent the different Euler angles of each volume element of the specimen with a 5 deg angular variation. Note that these Euler angles refer to specimen directions when inserted in the microscope and, therefore, do not generally correspond to the Euler angles conventionally used to describe a deformed material. In many cases, regions of similar orientation have similar colors; however, this is not always the case due to discontinuities in Euler space.[1] In order to remove the noise encountered at low misorientation angles, the representation of the high-, medium-, and low -angle boundary fractions are based on misorientations larger than 2 deg (step width = 2 deg).

For TEM, two to three 3-mm-diameter foils were punched from the center of the cross section of each of the ED samples. The thin electropolished foils were prepared in an electrolyte of 25 pct orthophosphoric acid, 25 pct ethanol, and 50 pct distilled water at 9 to 10 V, 20 °C with a current of ~150 mA. A PHILIPS[§] CM-20 transmission electron microscope operating at 200 kV was used to capture the bright-field (BF) images. Selected area diffraction (SAD) patterns were taken with an aperture diameter of 5.8 μm along the $<110>$ zone axis and at zero tilt of the double tilt specimen holder. Statistical measurements of the microstructural features were performed on at least four digitized negative films from each specimen at a magnification of times 27.5 K. In areas where characteristic microstructural features such as the LBs observed at higher passes were scarce, the statistics are lower. The sizes of approximately 150 to 200 cells were measured for each ECAE condition along two axes. When LBs were present, the cell size was measured parallel and perpendicular to this reference orientation.

Similar to EBSD, texture analysis was performed on $20 \times 20 \times 3$ mm^3 ED samples using a GBC-MMA texture goniometer working at 40 kV and 25 mA and equipped with a Cu K_α anode and a polycapillary beam enhancer, resulting in a collimated beam of 10×10 mm^2. Raw data in the form of incomplete pole figures (PFs) (χ = 0 to 80 deg) from the (111), (200), and (220) crystallographic planes were used to calculate the orientation distribution functions (ODFs) $f(g)$ using the spherical harmonic method without imposing any sample symmetry conditions. The equation $g = (\phi_1, \phi, \phi_2)$ refers to grain orientation denoted by the three Euler angles in Bunge's notation.[24] All *end*-texture PFs and ODFs were subsequently rotated to TD view and will be discussed in the *xyz* laboratory system (Figure 1). Correspondingly, the TD, ED, and ND axes are denoted along the ϕ_1, ϕ, and ϕ_2 directions, respectively.

III. RESULTS

A. *Microstructure and Grain Size Evolution*

1. *Measurements via EBSD*

After one pass (Figure 2(a)), elongated grains and subgrains are present. Here, the shear direction is out-of-plane, as indicated by the TD and ND directions. More than 80 pct of all boundaries are of LAGB configuration (Table I). The 80-nm step size measurements indicate that the ECD of grain size varies greatly and lies between 200 and 3000 nm. Grains are elongated along the shear direction and have a high aspect ratio (AR). The mean ECD subgrain size was 230 nm, with a more equiaxed shape. Comparatively, after $N = 4$ (Figure 2(b)), the grain size and subgrain size have reached their minimum values and a significantly higher volume fraction of HAGB has correspondingly developed. These values remained roughly constant thereafter, irrespective of increasing N (Table I). It must be noted that for $N \geq 4$, the difference between grain and subgrain size is significantly smaller than after a single ECAE pass and is also indicative of an increase in boundary misorientation angles. Furthermore Figures 2(b) through (d) also indicate a more equiaxed configuration compared to the more LB substructure after the $N = 1$. This change is also reflected in the AR values given in Table I.

After scanning the same specimens using two different step sizes of 80 and 40 nm, the EBSD results returned different values. Table I shows consistently smaller grain

[‡]HKL-Channel 5 is a trademark of Oxford Instruments, Oxfordshire, UK.

[§]PHILIPS is a trademark of Philips Electronic Instruments Corp., Mahwah, NJ.

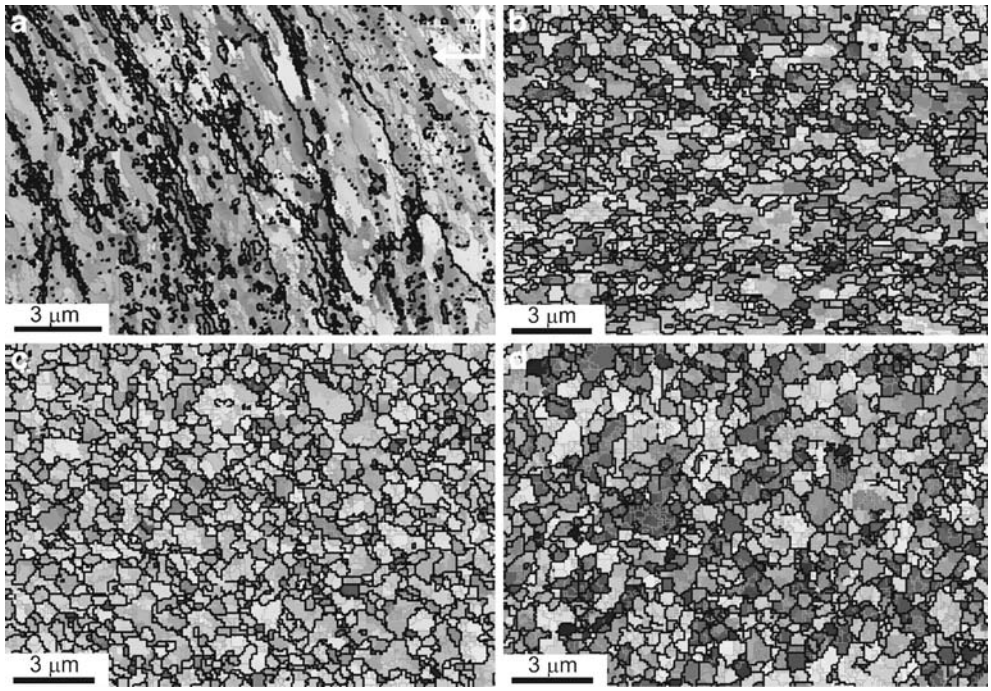

Fig. 2—EBSD maps of (*a*) $N = 1$, (*b*) $N = 4$, (*c*) $N = 12$, and (*d*) $N = 16$ passes represented by 256 colors, using a step size of 80 nm. The strengths of the primary colors are proportional to the three Euler angles. Thick lines highlight boundaries with misorientations > 15 deg (HAGB), while thin lines highlight boundaries with misorientations < 15 deg (LAGB).

and subgrain sizes when the smaller 40-nm step size is used. A similar tendency has been previously reported for highly strained metals.[1] However, when the calculated misorientation data for 80- and 40-nm step sizes were compared, no discernable difference was evident.

Examining the misorientation distribution with number of passes (Figure 3), we find that misorientations with angles smaller than 5 deg decrease steadily with increasing N. After the first pass, the least number of grains are found between misorientations of 20 to 30 deg (*i.e.*, medium-angle boundaries). With greater passes, and beyond the 30 deg angular range, the contribution of higher angle misorientation relationships increases. The decrease in fraction of LAGB with increasing N indicates a clear evolution from a large number of LAGBs per area (at $N = 1$) toward a smaller number of LAGBs in favor of HAGB formation. This is shown in Table I by the ratio of the total number of LAGBs to the total number of HAGBs, which decreases significantly from $N = 1$ to 4, but remains constant thereafter. Furthermore, a change in the amount of coincidence site lattice (CSL) boundaries is also observed. The percentage of Σ1 and Σ3 boundaries with respect to the number of intersecting boundaries according to (1) the Brandon criterion[25] and (2) as a fraction of that expected for a random grain assembly is presented in Table I. The Brandon criterion describes the maximum tolerance of misorientation angle ($\Delta\Theta$) from an exact CSL relationship by

$$\Delta\Theta = \Theta_m \Sigma^{-1/2} \qquad [1]$$

where Θ_m is the maximum misorientation angle for a low-angle boundary (typically, 15 deg). With higher N, the percentage of Σ1 and Σ3 boundaries decreases and increases, respectively. Boundaries with Σ values greater than 3 are below the 1 pct margin and are therefore of minor importance. Nevertheless, with increasing N, a greater abundance of high Σ-value boundaries for, *e.g.*, −Σ7, Σ13, and Σ19, which are regarded as being more mobile than others,[26] is also observed. Generally, a rise in the number of Σ3 boundaries can be ascribed to recovery and recrystallization mechanisms, which favor low-energy boundary configurations. Just such a micro-

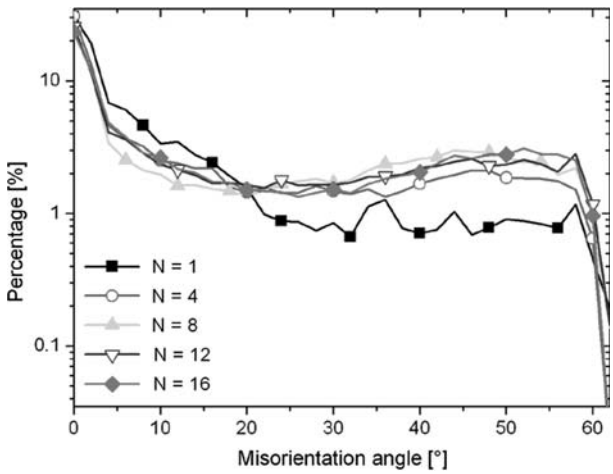

Fig. 3—Histogram of average grain boundary misorientation for copper after $N = 1$ to 16 passes ECAE processed *via* route B_C.

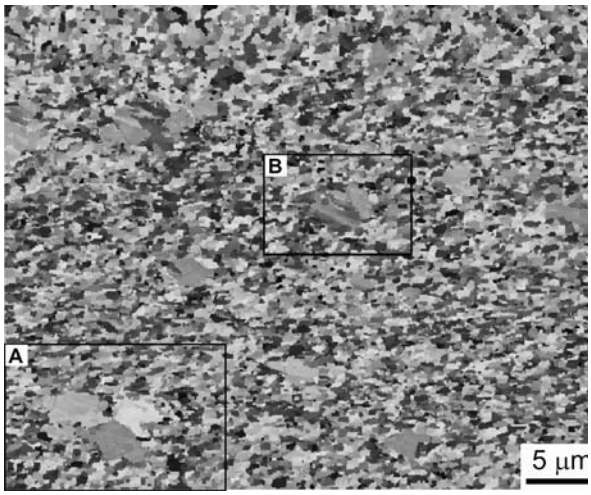

Fig. 4—Large EBSD map ($39 \times 32\ \mu m^2$) of a copper specimen subjected to $N = 16$ passes ECAE processed *via* route B_C.

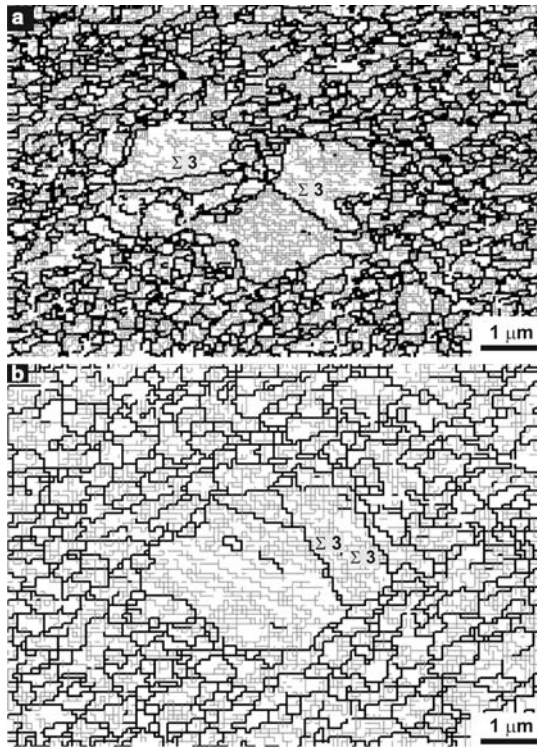

Fig. 5—(*a*) and (*b*) Enlargements of areas taken from the EBSD map shown in Fig. 4 outlining the HAGBs (thick lines) and the LAGBs (thin lines).

structure is shown in Figure 4, wherein a large scan area was chosen for the $N = 16$ pass specimen. The highlighted areas A and B in Figure 4 clearly show large grains (~1 to 4 μm in diameter) that exhibit a local abundance of Σ3 boundaries (the respective areas are magnified in Figures 5(a) and (b)). Their sizes are about 10 times larger than their immediate neighbors and the average grain size of the surrounding microstructure.

2. *Measurements via TEM*

In this section, the microstructural evolution observed by TEM-BF images and SAD patterns is described, which corroborates our previous work[22,27] on the same material, but provides a more complete picture particularly with respect to the EBSD results. As grain misorientations were not quantitatively measured, different criteria compared to EBSD measurements were applied for the definition of grain, subgrain, and cell size in accordance with the classification given in References 4 and 8 and briefly described in Section I. Grains were defined as such if confined by mainly sharp GBs bounded by qualitatively large misorientation angles. They were also easily distinguishable from other microstructural features by their larger size. Similarly, LBs are borders of large changes in misorientation, but in this case, these boundaries can exhibit significantly greater width, which is reflected by a high density of accumulated dislocations (= DDW). Subgrains and dislocation cells are indicated by diffusely scattered boundaries and confined to other subgrains or cells by lower misorientations. Different from dislocation cells, subgrains do in part show sharper boundaries, whereas cells are confined only by thick dislocation cell walls. Qualitatively speaking, this correlation was checked regularly while working on the TEM using a parallel beam for SAD (using the smallest diaphragm) or convergent beam diffraction. This is in agreement with quantitative TEM observations performed by Huang *et al.*,[28] who have shown a clear correspondence of the appearance of boundaries and their misorientation. In the measurements presented in Table I, they were not counted separately.

Parallel LBs oriented along the trace of the {111} planes with $<110>$ directions are the dominant microstructural feature in the specimen subjected to $N = 1$ (Figure 6(a)). Strongly elongated subgrains with a length of ~200 to 2000 nm are situated in-between the LBs. Within the subgrains, smaller, more equiaxed cells are present. The SAD pattern also shows the presence of strong texture components (*i.e.*, preferred orientations) oriented along the $<110>$ direction. After $N = 4$, while a more equiaxed microstructure is dominant and accounts for nearly 70 pct of the entire specimen volume, strong localized inhomogeneities with intact or truncated LBs were also observed. Just such a "mixed" microstructure is also shown in Figure 6(b) wherein the lower part reflects the equiaxed grain structure while the upper part shows the persistence of a more elongated subgrain structure. With increasing N, a more equiaxed subgrain/grain structure evolves, due to subgrains with initially low misorientation angles rotating and transforming into grains with higher misorientation angles.

After $N = 12$ and 16, the microstructure is fairly homogeneous (Figures 6(c) and (d)) with slip lines from previous passes no longer visible. The subgrains are mainly equiaxed and the appearance of the microstruc-

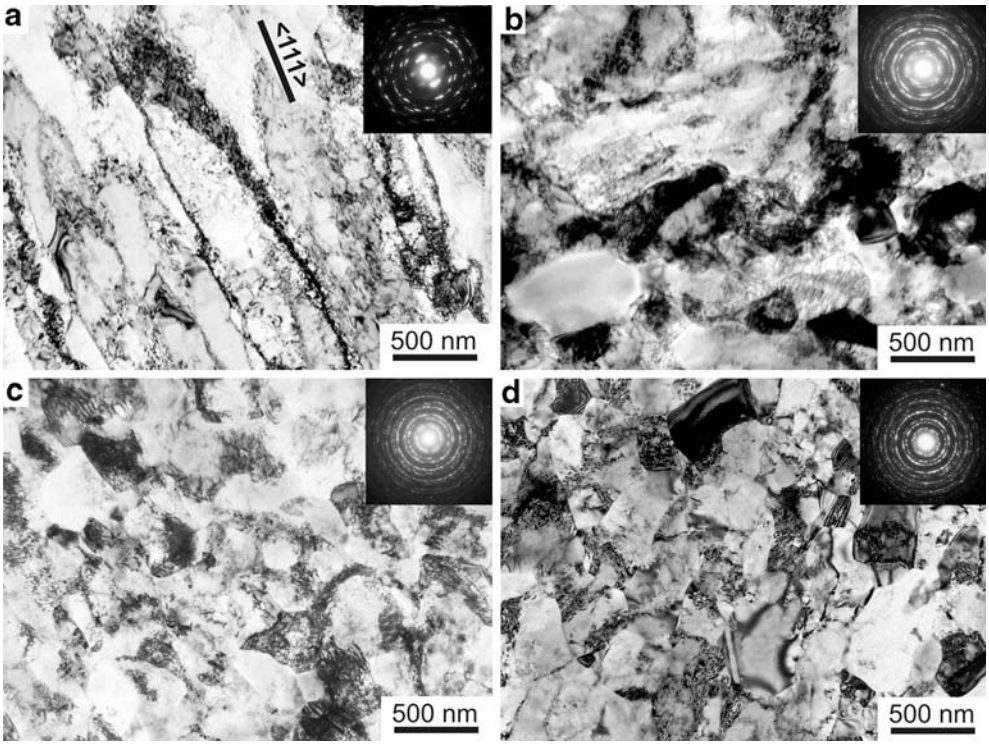

Fig. 6—TEM-BF images and SAD patterns (inset) of copper after $N = 1$, 4, 12, and 16 passes.

ture for both specimens does not change laterally along the thin TEM foil. The few elongated grains found in the specimens after $N = 12$ did not show any preferential orientation in the ED plane. A comparison of the SAD patterns for $N = 12$ and 16 conditions presented as insets in Figures 6(c) and (d) shows a more random misorientation for the former and distinct spots for the latter condition. Qualitatively, the $N = 16$ pass specimens appeared to contain a greater fraction of HAGBs and also a larger degree of recovery, evident as lower dislocation densities within the grains (Table I). Furthermore, the degree of relaxation was compared semiquantitatively by counting the number of "sharp" boundaries normalized over an area of approximately 10 μm^2. These sharp (and often straight) boundaries confine crystal areas, where a strong change in the diffraction pattern occurs. They are generally considered to (1) be of high-angle misorientation, (2) to enclose grains of low dislocation densities, and (3) to be larger than the surrounding grains/subgrains. This would indicate that the strain field caused by these boundaries is of low intensity and that they are, in effect, in a state closer to equilibrium than cell wall boundaries. This, in turn, gives rise to sharp diffraction spots in the SAD. The appearance of such grains is typical for recovery mechanisms and is in agreement with the EBSD observations presented in Section A–1.

The subgrain/cell sizes decrease between $N = 1$ and 4 and remain constant thereafter for higher N (Table I). However, at the same time, the boundary wall width also decreases with increasing N. Oftentimes smaller dislocation-free domains were found within cells, which are confined by a dislocation network built up by only a few dislocations. These could represent the first stage of newly evolving cell walls. Figure 7(a) shows the prevalence of such domains within a grain, each confined by single dislocations. A further indication of relaxation processes occurring at higher N is also the increasing abundance of boundaries assimilating twin boundaries or stacking faults, as shown in Figure 7(b), again in agreement with the observations made by EBSD.

3. *Measurements via XRD peak broadening*

The full-width at half-maximum from diffraction peaks of the (111) and (222) planes, coherent domain size, and the lattice strain in the ECAE-processed Cu specimens were calculated after each pass (Table I). As shown in Table I, while the domain size remains constant with increasing N, the lattice strain decreases. Moreover, these values are significantly smaller than those measured by TEM and EBSD. In materials where dislocations produced by lattice strain effects are limited (as in the case of nanocrystalline electrodeposited specimens), a good correlation between grain size measured by TEM and XRD can be reached.[17] However, in highly strained materials such as the present ECAE-Cu case, a coherent domain size rather than a grain size is measured and returned by XRD. This, in turn, alludes to the presence of even smaller substructures within the cells. Thus, the measured distance between dislocation structures shown in Figure 7(a) fits reasonably well within the coherent domain

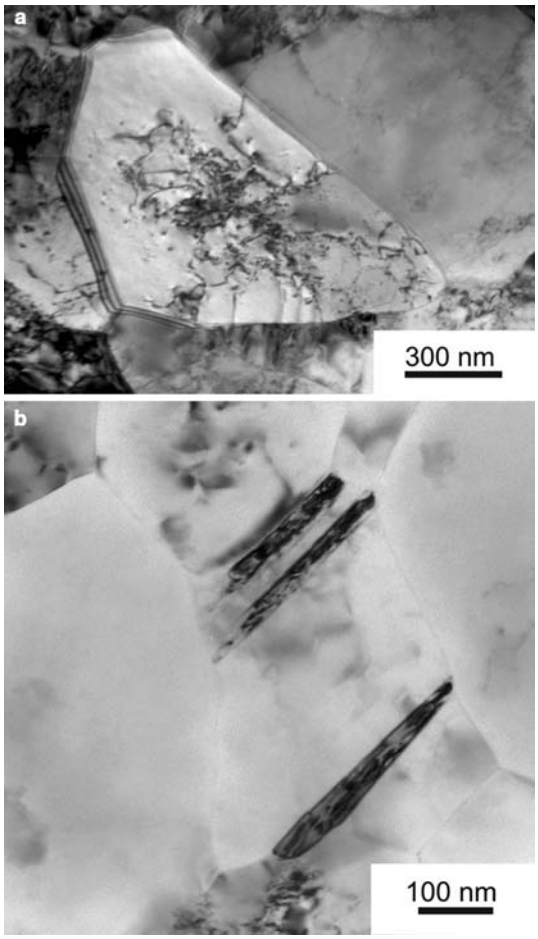

Fig. 7—(*a*) Observed dislocation network within copper grains and (*b*) boundaries assimilating a twin or stacking fault relationship recorded in a sample subjected to $N = 16$ passes.

sizes measured by XRD. Similar values for the domain sizes in ECAE-deformed Cu have been measured using an HR diffractometer.[29]

B. *Multipass ECAE Texture Evolution*

Figure 8(a) denotes the (111) experimental PF prior to ECAE. Similar to a previous study,[30] the initial texture is weak and consists of a $<111> + <001>$ duplex fiber with the fiber axis parallel to the billet longitudinal axis.

According to the convention adopted from Reference 31, ECAE texture orientations can be derived for the condition of *negative* SS by increasing the ϕ_1 Euler angle by the half angle of die intersection (in this case, $\theta = \Phi/2 = 45$ deg) while keeping the ϕ and ϕ_2 angles constant. Thus, the $\{111\}$ and $<110>$ partial fibers characteristic of fcc materials can be reclassified as $\{111\}_\theta$ and $<110>_\theta$ types by 45 deg CCW rotation around the TD and away from the ND plane and ED, respectively.[31] Similarly, the Euler angles and Miller indices of the ideal SS orientations are denoted in Table II, and their ideal positions on the (111) key PF and the ODFs are shown in Figures 8(b) and 9, respectively.[31]

As seen in Figure 8(c), the $N = 1$ pass (111) experimental PF contains dyadic symmetry and depicts an inversion center projected onto the z plane. It consists of a partial $<110>_\theta$ fiber running from C_θ to $A_\theta/\bar{A}_\theta$ ("/" denotes "or") through $B_\theta/\bar{B}_\theta$ orientations and a partial $\{111\}_\theta$ fiber extending from $A^*_{1\theta}$ to $A^*_{2\theta}$ through $A_\theta/\bar{A}_\theta$. Relatively high orientation densities can be found near the $C_\theta$and $A^*_{1\theta}$ components. Similar to Reference 31, a stronger $A^*_{1\theta}$ component compared to $A^*_{2\theta}$ is a direct result of negative SS. Overall, the present texture components after $N = 1$ are closely aligned to the ideal ECAE orientations.

Furthermore, Li *et al.*[31,32,33] have shown that $N = 1$ pass ECAE texture components are characterized by orientation concentrations along three fibers designated as f1, f2, and f3 and are indicative of monoclinic sample symmetry with the TD axis (or, equivalently, the ϕ_1 direction) being the dyad axis (Figure 9(a)). A short description of the orientation components along any fiber is given subsequently. The f1 fibers comprise $A^*_{1\theta} - A_\theta/\bar{A}_\theta - A^*_{2\theta}$ orientations and consist solely of the $\{111\}_\theta$ partial fiber. The f2 fibers run along $C_\theta - \bar{B}_\theta/B_\theta - \bar{A}_\theta/A_\theta - A^*_{1\theta}$ and comprise both the $C_\theta - \bar{B}_\theta/B_\theta - \bar{A}_\theta/A_\theta$ or $<110>_\theta$ and the $\bar{A}_\theta/A_\theta - A^*_{1\theta}$ or $\{111\}_\theta$ partial fibers, respectively. Symmetrical to the f2 fiber, the f3 fiber contains the $C_\theta - \bar{B}_\theta/B_\theta - \bar{A}_\theta/A_\theta - A^*_{2\theta}$orientations, which can be subdivided into the $C_\theta - \bar{B}_\theta/B_\theta - \bar{A}_\theta/A_\theta$ or $<110>_\theta$ and the $\bar{A}_\theta/A_\theta - A^*_{2\theta}$ or $\{111\}_\theta$

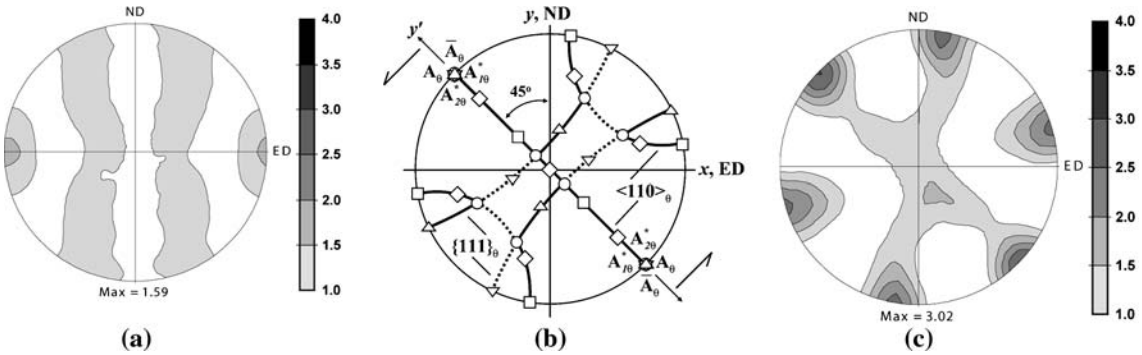

Fig. 8—(111) pole figure of the (*a*) $N = 0$ pass starting experimental texture for Cu (the longitudinal axis of the billet is horizontal), (*b*) ideal orientations (symbols) and partial fibers (thick solid lines) after $N = 1$ pass ECAE deformation for fcc materials using a $\Phi = 90$ deg die, and (*c*) $N = 1$ pass experimental texture.

Table II. Ideal Orientations of Important Simple Shear Texture Components Observed in the $\phi_2 = 0$ and 45 Deg Sections of Orientation Distribution Functions for Fcc Metals after $N = 1$ Pass ECAE Adapted from Reference 31

	Euler Angles (Deg) for $\phi_2 = 0$ and 45 Deg Sections			Miller Indices			
Notation	ϕ_1	Φ	ϕ_2	ND (Approximately)	ED (Approximately)	TD	Fiber Family
$A^*_{1\theta}$	80.26, 260.26	45	0	$[8\ 1\ \bar{1}]$	$[1\ \bar{4}\ 4]$	[0 1 1]	$\{111\}_\theta$
	170.26, 350.26	90	45				
$A^*_{2\theta}$	9.74, 189.74	45	0	$[1\ \bar{4}\ 4]$	$[8\ 1\ \bar{1}]$	[0 1 1]	$\{111\}_\theta$
	99.74, 279.74	90	45				
A_θ	45	35.26	45	[9 1 4]	$[1\ \overline{11}\ \bar{5}]$	$[\bar{1}\ 1\ 2]$	$\{111\}_\theta$, $<110>_\theta$
$\bar{A}_\theta$	225	35.26	45	$[\bar{1}\ \overline{11}\ 5]$	$[\bar{9}\ \bar{1}\ \bar{4}]$	$[\bar{1}\ 1\ 2]$	$\{111\}_\theta$, $<110>_\theta$
B_θ	45, 165, 285	54.74	45	[15 4 11]	$[7\ 26\ \overline{19}]$	$[\bar{1}\ 1\ 1]$	$<110>_\theta$
$\bar{B}_\theta$	105, 225, 345	54.74	45	$[\bar{7}\ \overline{26}\ 19]$	$[\overline{15}\ \bar{4}\ \overline{11}]$	$[\bar{1}\ 1\ 1]$	$<110>_\theta$
C_θ	135, 315	45	0	[3 3 4]	$[2\ 2\ \bar{3}]$	$[\bar{1}\ 1\ 0]$	$<110>_\theta$
	45, 225	90	45				

partial fibers, respectively. Again, after a single-pass ECAE (Figure 9(a)), approximately uniform orientation densities are observed along all three fibers with the developed orientations close to their ideal positions. Analogous to the PF (Figure 8(c)), and similar to previous results,[33] while moderate strengths are observed for $A^*_{1\theta}$, $A_\theta/\bar{A}_\theta$, and $\bar{B}_\theta/B_\theta$ components, slightly stronger intensity was seen for the C_θ orientation and comparatively weaker intensity was recorded for the $A^*_{2\theta}$ component.

After four passes (Figure 9(b)), the near-monoclinic sample symmetry along the fibers between $\phi_1 = 0$ to

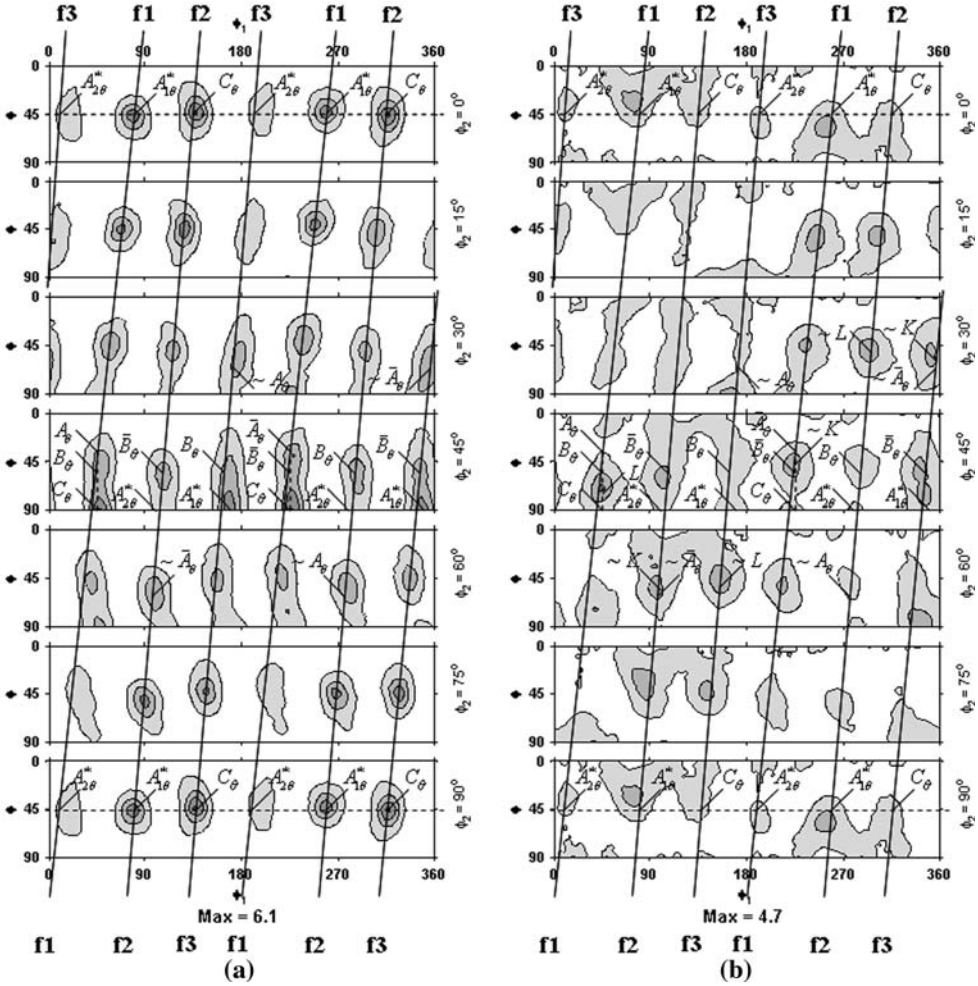

Fig. 9—ϕ_2 = constant ODF sections of copper after (*a*) $N = 1$, (*b*) $N = 4$, (*c*) $N = 8$, (*d*) $N = 12$, and (*e*) $N = 16$ passes ECAE processed *via* route B_C. Contour step size: 1.65 times.

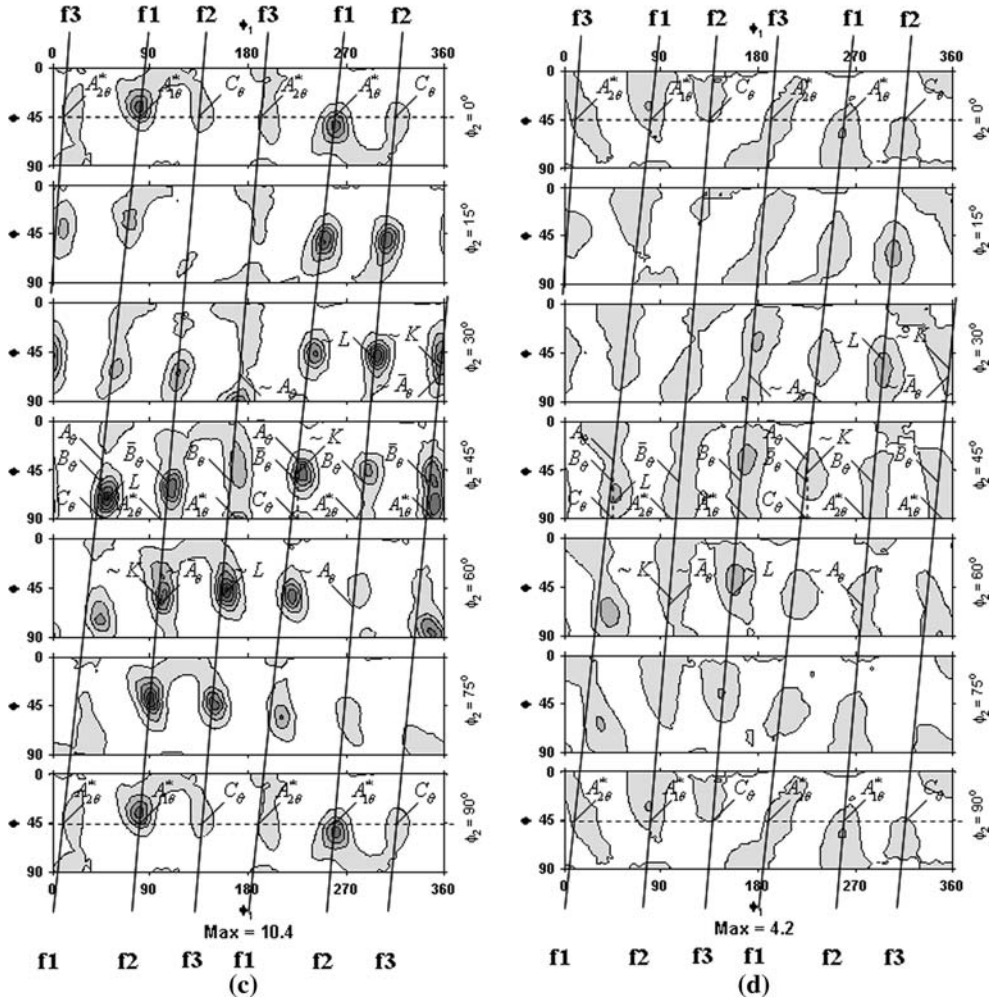

Fig. 9—continued.

180 deg and ϕ_1 = 180 to 360 deg is destroyed. The f1 and f3 fibers appear incomplete and less uniform as orientation densities differ and also result in an overall reduction in maximum texture intensity ($f(g)$). In agreement with Reference 33, the appearance of orientations at intermediate positions, (1) near the ideal $\bar{A}_\theta$ component and (2) between B_θ and C_θ components (denoted as K $(\bar{6}23)[03\bar{2}]$ and L $(2\bar{1}\bar{2})[1\bar{2}2]$, respectively) are readily apparent after four passes. As a direct consequence of further processing, minor peaks belonging to retained components from previous passes are also observed. Compared to the one-pass specimen, the end of $N = 4$ results in significant weakening of intensities around the $A^*_{2\theta}$ and C_θ components accompanied by moderately stronger $A^*_{1\theta}$, K, and L components.

When comparing the relative strengths of orientation densities among the various components after $N = 8$ (Figure 9(c)), the results are similar to $N = 4$ with comparatively lesser $f(g)$ recorded for intensities around $A^*_{2\theta}$ and C_θ. However, despite the reproducibility in texture components, large disparities in the orientation of the texture components do exist. In contrast to the $N = 4$ condition, $N = 8$ resulted in an overall increase in $f(g)$. Moreover, a further strengthening of $A^*_{1\theta}$ and $\bar{B}_\theta$ orientations occurs at locations slightly shifted away from their ideal orientation positions (in the positive ϕ_1 direction), while the maximum $f(g)$ are recorded at the $\sim K$ and $\sim L$ orientations. Similar to the $N = 4$ and in contrast to the $N = 8$ condition, the texture after 12 passes (Figure 9(d)) exhibits a weak overall maximum texture intensity. Also, by this stage, the most notable difference in terms of orientation densities between $N = 4$ and 12 is that greater strain produces a net spread of orientation components. Texture intensities from $N = 12$ to 16 passes (Figure 9(e)) indicate a slight increase in maximum $f(g)$. When comparing the relative strengths of the various orientation components with respect to each other, the results are similar to all previous ECAE passes because the $A^*_{1\theta}$, $\bar{B}_\theta$, B_θ, K, and L components are approximately equivalent in strength while comparatively weaker $A^*_{2\theta}$ and C_θ components are present. In terms of their locations on the ODF, the shear-type texture components remain slightly shifted away from their ideal positions but, conversely, still indicate a greater spread in orientation density as a consequence of previous processing.

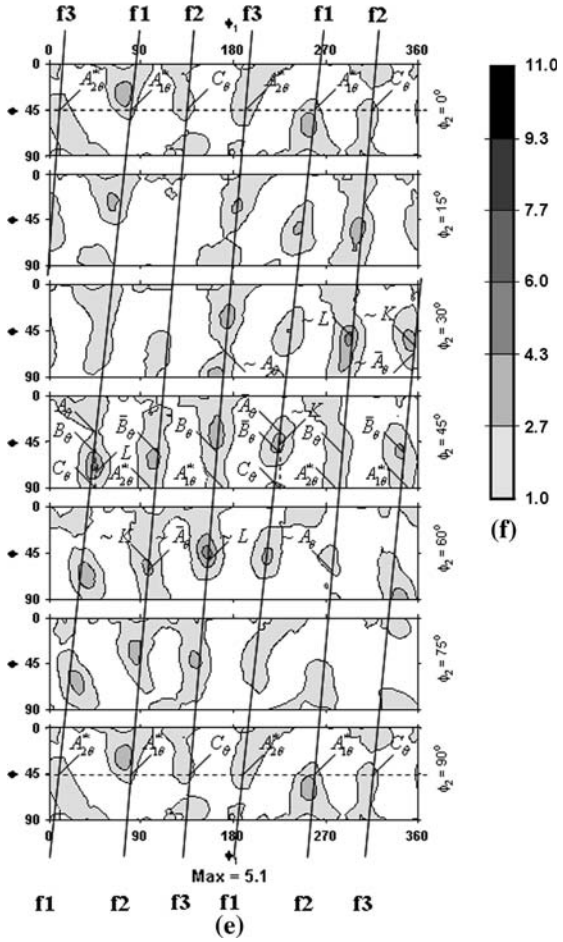

Fig. 9—continued.

IV. DISCUSSION

A. *Grain Size Measurements*

The size measurements performed by XRD, EBSD, and TEM provide a deeper insight into the complexity of the microstructural evolution during ECAE. The ECD measurement is related to the true grain diameter $\overline{D}$ by[1]

$$\mathrm{ECD} = 0.816\,\overline{D} \qquad [2]$$

In this respect, EBSD-ECD size measurements presented in Table I are an underestimate, which would result in approximately 20 pct larger *actual* grain diameters. Furthermore, scans with an 80-nm step size on the $N = 4$, 8, 12, and 16 specimens returned consistently larger grain sizes than the 40-nm step size scans. This correlation has previously been observed[1] and occurs due to the omission of misorientations during the experiments with a higher step size. This effect is enhanced when lower indexing rates are achieved due to the presence of large grain boundary volumes. Hence, fewer misorientation changes are detected with the coarser step size, resulting in larger grains and subgrains.

In a recent EBSD investigation by Vinogradov *et al.*[34] on pure Cu processed *via* route B_C for $N = 16$ and 20 passes, a step size of 40 nm yielded an ECD of 400 to 500 nm on the flow (or ND) plane. Compared to the results presented here, the difference in grain size is probably not from extrinsic measurement and postprocessing variables (listed in Reference 1) as the possible sources of differences, but rather, it reflects the nature of the three-dimensional grain shape produced by route B_C after multiple passes. Within the ND plane, grains are commonly more elongated (with measured ARs of 2.5[35]) and may result in a larger ECD for HAGBs compared to those in the ED plane.[34] The close agreement of yield strengths in their material and the values given in Table III confirm this assumption. A larger AR for planes parallel to ED compared to those perpendicular has been also noted by TEM in other ECAE-processed metals.[36–39]

In summary, it can be concluded that grain size decreases strongly from $N = 1$ to 4 and is approximately stable for greater numbers of passes. On the other hand, the subgrain size has already reached its minimum value after $N = 1$ and remains roughly constant through all subsequent passes. According to TEM observations, a strong drop is observed for the microband spacing between $N = 1$ and 4, which is in agreement with the EBSD measurements and indicates that microbands are separated by HAGBs. Conversely, the TEM subgrain/cell size shows only small decreases from $N = 1$ to 4 and reaches a minimum value of about 220 nm. This value is in agreement with literature values given for subgrain sizes measured by TEM.[40–43] Similarly, a decrease in the grain size and a steady subgrain size with increasing N has also been observed in Al and IF steel.[44,45]

Taking Eq. [2] into account, the grain size and subgrain size measured with the 40-nm step size are in close agreement with the values measured by TEM. In this respect, the comparison shows that the shortest visible boundary spacing of dominant TEM diffraction contrasts, *i.e.*, originating from cell walls, subgrain boundaries, or GBs, can be taken as a measure for boundaries that are confined by LAGB. With increasing strain ($N > 4$), the microstructure experiences relaxation and recovery effects, which on the one hand are reflected by the local increase in sub-/grain-cell size (Figures 4, 6(d), and 7(a)), decrease in the boundary wall width, and increase in equilibrium GBs observed by TEM and, on the other hand and on a smaller scale, by the increase in the coherent domain size and decrease in microstrain measured by XRD peak broadening (Table I). A similar microstructural evolution in ECAE-UFG-Cu observed in TEM is described by Huang *et al.*[28] In our previous work, we have interpreted this effect as a sign for an increase in the mean free path of dislocations and correlated it with the decrease in the yield strength (YS) after $N = 8$.[22] It is suggested that these processes occur simultaneously along with the increase in misorientation angle among subgrains, which is again part of the recovery mechanism involving dislocations in the cell wall, which rearrange themselves in order to screen the long-range stress field.[11,46] While the observation of 1- to 4-μm large grain aggregates (Figure 4) after $N = 16$ does not

Table III. Experimental and Calculated Microstructure and Mechanical Characteristics for Copper after $N = 0$, 1, 4, 8, 12, and 16 Passes

Microstructure and Mechanical Characteristics	Number of Passes					
	$N = 0$	$N = 1$	$N = 4$	$N = 8$	$N = 12$	$N = 16$
Experimental						
$\overline{\Theta}$ (< 15 deg)	NA	6.0	6.2	5.8	6.2	6.2
$\overline{\Theta}$ (> 15 deg)	NA	37.1	39.4	40.5	40.5	41.5
d_{LAGB}*	NA	NA	230	180	190	180
total dislocation density (m^{-2})	NA	$1.9 \pm 0.9 \times 10^{14}$	$3.2 \pm 1.4 \times 10^{14}$	$2.1 \pm 1.8 \times 10^{14}$	$1.3 \pm 1.1 \times 10^{14}$	$6.9 \pm 0.7 \times 10^{13}$
cell dislocation density (m^{-2})	NA	$1.6 \pm 0.9 \times 10^{14}$	$2.8 \pm 1.4 \times 10^{14}$	$2.0 \pm 1.8 \times 10^{14}$	$1.2 \pm 0.3 \times 10^{14}$	$6.4 \pm 0.7 \times 10^{13}$
wall dislocation density (m^{-2})	NA	$1.5 \pm 0.2 \times 10^{15}$	$2.5 \pm 0.8 \times 10^{15}$	$1.9 \pm 0.5 \times 10^{15}$	$2.1 \pm 0.7 \times 10^{15}$	$1.5 \pm 0.4 \times 10^{15}$
yield strength (0.2. pct) (MPa)	68 ± 6	342 ± 5	415 ± 4	385 ± 3	348 ± 4	345
UTS (MPa)	332 ± 13	358 ± 2	455 ± 4	449 ± 1	423 ± 8	407
Calculated						
$\sigma = \frac{k_1}{\sqrt{d}}$ Eq. [2]						
EBSD*						
ECD grain (MPa)	NA	NA	298	292	340	321
ECD subgrain (MPa)	NA	NA	404	388	404	404
d_{LAGB} (MPa)	NA	NA	292	330	321	330
TEM (MPa)	NA	298	340	345	340	298
XRD (MPa)	NA	572	586	562	525	572
$\sigma = \frac{M\alpha G}{\sqrt{1.5bS_f\Theta}}$(MPa)	NA	NA	936	1026	1028	1054
σ *via* Eq. [6] for ρ_t (MPa)	NA	174	225	183	145	105
σ *via* Eq. [7] for $\rho_t = \rho_i + \rho_c$		340	623	552	557	467

*40-nm EBSD step size

significantly change the mean grain size value due to the small number of such large grains, a non-negligible volume fraction *may* influence the final mechanical properties. Indeed, the lower YS measured in $N = 8$, 12, and 16 specimens may be also explained by the presence of such recovered deformation substructures.[22]

B. *Grain Boundary Characteristics*

On a microscopic scale, the GB characteristics measured by EBSD show that misorientation angles change significantly up to $N = 4$ but remain roughly constant for higher N (Figure 3). In more detail, EBSD measurements indicate a maximum fivefold increase in the 35 to 60 deg misorientations between $N = 1$ to 16. Nonetheless, passes ≥8 still show a significant fraction of LAGB (more than 50 pct). This can be explained if changes in grain and subgrain size are accounted for. The grain size decreases steadily up to eight passes, while the subgrain size already shows minimum values after the first pass and is, by comparison, less than half the grain size. Hence, two to three LAGBs are incorporated within one grain, which accounts for the larger fraction of LAGBs (than HAGBs) between $N = 1$ to 8. A similar observation on ECAE-Cu processed up to $N = 8$, route B_C has been observed by TEM misorientation measurements for grains and subgrains.[5]

Comparison of the present values with other recent TEM and EBSD investigations on ECAE-processed metals shows similar results for misorientation relationships and the increasing amount of HAGB population with increasing N.[5,34,35] The EBSD measurements performed on the ND plane of pure Cu samples processed by route B_C for 16 and 20 passes show HAGB fractions of 67 to 71 pct.[35] On the other hand, TEM misorientation measurements on the same plane of the Cu samples processed up to $N = 8$, route B_C show only 27 pct HAGBs.[5] The variations in results from both the literature and the present misorientation measurements might be alluding to the difficulty of detecting boundaries of subgrains and grains that are below the detection limit (sizewise and misorientation-wise). In particular, this is especially challenging for LAGBs, because they are more closely spaced and their misorientations can be very low. For instance, early TEM misorientation measurements often showed overestimated fractions of HAGBs due to the misinterpretation of the SAD patterns and BF images.[47] On the other hand, EBSD measurements with very large step sizes also lead to an overestimation of the HAGB fraction by disregarding some LAGBs.

The Brandon criterion[25] determines the maximum tolerance of misorientation angle ($\Delta\Theta$) for $\Sigma1$ and $\Sigma3$ boundaries as 15 and 8.7 deg, respectively (Eq. [1]). Therefore, the higher the numerical value of the Σ boundary, the smaller is the percentage of the microstructural volume fraction associated with it. Nonetheless, the observed trend for the $\Sigma1$ and $\Sigma3$ boundaries between $N = 1$ to 16 is correct if compared with the misorientation distribution presented in Figure 3. However, it remains unclear whether the $\Sigma3$ boundaries shown in Figure 5 realistically reflect an increasing abundance of symmetric twin boundaries or just depict orientations close to the $\Sigma3$ boundaries. The

TEM investigations have shown that at higher N, microstructures assimilating twin boundaries or stacking faults become more abundant. Note that the boundaries observed in Figure 7(b) have not been indisputably identified as being either twin boundaries or stacking faults. However, recent HR-TEM enabled the identification of deformation twins in Cu specimens deformed by ECAE up to $N = 24$.[48] Furthermore, Σ3 boundaries have not been explicitly observed for symmetric tilt boundaries (twins) but have also been previously connected to stacking faults in fcc materials.[49] Because Σ3 boundaries were found to be locally associated with the occurrence of significantly larger grains, this change in the boundary character is assumed to be related to thermally activated recovery processes. Note that larger recrystallized areas have also been observed by EBSD in ECAE ($N = 3$ and 5) of single-crystal Cu measured 2 months after processing.[50] Because recovery processes are temperature sensitive, it can be assumed that with increasing temperatures, a higher number of these boundaries would evolve. In fact, TEM investigations on 423 and 473 K annealed specimens confirm the high twin density in such Cu samples.[51]

C. *Application of the Alternative Hall–Petch Relationship*

After having obtained a detailed view of the microstructural characteristics of ECAE-Cu samples, a better understanding of the microstructural evolution with strain on the mechanical properties can be derived. In this section, the hardening mechanisms of ECAE-Cu in terms of the classical Hall–Petch relationship[13,14] have been discussed and compared to a modified Hall–Petch equation recently proposed for highly deformed microstructures.[12]

Mechanical property data are presented in Table III along with the other additional microstructural parameters used in the equations below. Details on the mechanical testing of the samples are given in Reference 22. The yield stress (σ_y) is related to the grain size (d) by[13,14]

$$\sigma_y = \sigma_0 + k_1 d^{-1/2} \qquad [3]$$

where (σ_0 = ~20 to 40 MPa) is the frictional stress required to move a dislocation in a single crystal, (k_1) is a constant, and the grain size (d) is assumed to be confined by HAGBs. As pointed out by Hansen,[12] the flow stress (σ) at a particular strain (ε) is given by

$$\sigma(\varepsilon) = \sigma_0(\varepsilon) + k_1 d^{-1/2} \qquad [4]$$

The strengthening contribution within the grain interior ($\sigma_0(\varepsilon)$) is thus very much dependent on the configuration and density of the dislocations accumulated in the material during the course of deformation resulting in the formation of cell walls. Hansen suggests that this strengthening could satisfactorily be described by the formation of mixed twist/tilt boundaries, wherein the dislocation density is a function of the misorientation angle (Θ). Thus, Eq. [4] could be rewritten as

$$\sigma(\varepsilon) = \sigma_0 + M\alpha G\sqrt{1.5bS_V\Theta} + k_1(\varepsilon)d^{-1/2} \qquad [5]$$

where M is the Taylor factor; α is a constant of ~0.33; b is the Burgers vector (=0.256 nm); G is the shear modulus (=48.3 GPa); and S_V is the area of boundaries per unit volume, which can be approximated by $S_V = 2/d_{\mathrm{LAGB}}$ (with d_{LAGB} being the inverse of LAGB spacing, Table III).[§][12]

[§]In addition, the mean linear intercept grain size was also calculated from the mean orthogonal boundary intercept spacing measured in both principal directions.

As deformation proceeds, boundaries that are described by the second term of Eq. [5] gradually transform from their LAGB character into HAGBs and can be treated in the same way as original GBs. In this respect, the second term in Eq. [5] is used for all LAGBs with misorientations <15 deg, while the last term accounts for the strengthening of HAGBs (≥15 deg). According to Hughes *et al.*,[8] the second term in Eq. [5] is related to the total dislocation density (ρ_t) by

$$\rho_t = \rho_i + 1.5S_V\Theta/b \qquad [6]$$

where (ρ_i) is the dislocation density in the volume between the boundaries. The second term is described by a relationship for the dislocation density in low-angle mixed twist/tilt boundaries, where the dislocation density is proportional to the dislocation spacing ($\mathbf{b}/\Theta$). Table III shows the dislocation density measured by TEM within the grains and the boundaries irrespective of the degree of misorientation. Inserting the measured values from Table III into Eqs. [5] and [6] shows that the second term in Eq. [5] reveals an unrealistically high yield strength compared to the measured one. Solving Eq. [6] for $d_{\mathrm{LAGB}} = 2/S_V$ by inserting the dislocation density measured in the cell walls would result in values of 500 to 800 nm for d_{LAGB}, which in turn would bring the calculated YS down to more realistic values.

However, a better correlation is achieved by simply inserting into Eq. [3] the ECD subgrain size, the d_{LAGB} spacing both measured with the EBSD step size of 40 nm, or inserting the TEM subgrain size (Table III). This reveals that ECAE-UFG-Cu still contains a significant amount of LAGBs, which due to their closer spacing than HAGBs determine the overall mechanical behavior without showing much sensitivity on the misorientation. In this respect, it can be assumed that Eq. [5] is only valid for a microstructure that exhibits a larger LAGB intercept length than the HAGB spacing. If so, the second term in Eq. [5] would be sufficiently small and would add to the stronger influence of the HAGB spacing. Such is the case in UFG-Al, which had been annealed to different temperatures and showed increased correspondence with Eq. [5].[2]

Furthermore, LAGBs in deformed crystals cannot be compared with those typical of undeformed metals (such as mixed twist and tilt boundaries) but contain a much higher concentration of dislocations over a larger boundary width.[22] Such boundaries have been called "nonequilibrium" boundaries and contain, in addition to the geometrical necessary dislocations, *excess* grain boundary dislocations,[52] which are assumed to act as strong obstacles for dislocation motion. Disregarding boundary strengthening, the Taylor equation written as

$$\sigma = M\alpha Gb\sqrt{\rho} \qquad [7]$$

can be used to evaluate the influence of the measured total dislocation densities and that of the cell interiors and cell walls. Inserting the values given in Table III for the total dislocation density by linearly adding $\rho_t = \rho_i + \rho_w$ according to Eq. [6], ($\rho_w \propto b/\Theta$)(similarly results in higher values compared to the experimentally measured YS. Therefore, a linear summation of the two dislocation densities is justified only if (ρ_w) arises exclusively from symmetric tilt/twist boundaries of low misorientations. However, lower YS values are estimated if the measured total dislocation density is inserted. This is probably associated with the common underestimation of dislocation densities measured by TEM, wherein only visible dislocations are counted and therefore represent the lower limit.[22] In fact, recent HR-XRD peak profile analysis on ECAE-processed Cu up to eight passes indicates that dislocation densities increase from $N = 1$ to 8 from 8×10^{14} to 26×10^{14} m^{-2} with a peak maximum after $N = 4$.[29]

The comparison of differently calculated YS values suggests that the misorientation angle of boundaries is not the critical parameter to evaluate the YS in ECAE-Cu, but in fact, the YS can be more adequately described by evaluating the spacing between cell walls or subgrain boundaries. A similar conclusion is arrived at by Li *et al.*,[20] where it was pointed out that the low-angle subgrain size controls the mechanical behavior *only* if it is significantly smaller than the high-angle grain size. Approximations of the different contributions to the YS according to the Taylor equation using calculated or measured dislocation densities are difficult because (1) densities measured by TEM may lead to an underestimation of the real densities and (2) peak broadening analysis does not provide local variations in dislocation densities (*i.e.*, in the cell wall and cell interior) and also are limited in the differentiation between cell walls, subgrain boundaries, or GBs.

D. *Texture Evolution*

As observed previously, the texture of ECAE-processed fcc metals can be adequately compared with the texture obtained by simple shear (or torsion[53]), although clear differences still exist between these two cases.[30,31]

Remembering that we can transpose bcc and fcc cubic crystal systems by exchanging their respective *hkl* and *uvw* Miller indices,[45,54] the ECAE textures can be compared to the texture evolution in α-iron and IF steel deformed *via* torsion.[55] This work concluded that the "tilt" (or rotation) phenomena indicates a trend wherein the ideal orientations are rotated around the specimen *z*-axis in the antishear direction (or negative ϕ_1 direction) at low strains ($\varepsilon < 1$) and, conversely, in the direction (or positive ϕ_1 direction) of shear at larger strains ($\varepsilon \geq 4$).[55] At intermediate strains ($1 < \varepsilon < 4$), the ideal orientations pass through their symmetry positions and would not indicate any tilt for this entire range of imposed strain.[55]

If these observations are applicable to ECAE, the so-produced texture components should likewise not tilt (or rotate) away from their ideal SS positions at least up to $N = 4$ passes.* In the present study, $N = 1$ yields ECAE orientations close to their ideal positions.[54] However, slight shifts in the positive ϕ_1 direction are discernable from $N = 4$ passes onward. Aside from postprocessing errors, Tóth *et al.*[56,57] stated that a rigid body rotation was inherent in SS-type deformation. Specific to the case of ideal SS (such as torsion), the number of operative slip systems is limited resulting in an overall negation of the tilt effect for the intermediate strain range.** [58] Contrarily, in the ECAE case, the operation of multislip from the first pass and onward (as seen in previous viscoplastic self-consistent modeling results[30,33]) causes the texture components to rotate (up to 10 deg) *in* the direction of the rigid body rotation.[59] As a result, (1) slip system activity coupled with (2) differences in entry texture due to a prescribed route and (3) the deformation necessitated by additional passes leads to variations in the orientation position (or "stability") of individual ideal components within the bulk texture.[59]

Our texture measurements agree with Baik *et al.*[60] on the overall reduction of the texture intensities for route B_C from $N = 1$ to 4. However, this trend is in contradiction with other investigations,[33,61] where an increase in texture strength after $N = 4$, 8, and 12 was found. Mainly, these disparities allude to the heterogeneity of the as-deformed billet due to varying friction conditions at the billet-die interface[32,62] and also the degree of difficulty in locating the exact center of the billet stable length (from where the ED plane sample is cut) for equivalently similar texture scans with increasing *N*. However, other differences such as (1) the starting texture of the material at $N = 0$[63] and (2) the area of the sample over which the texture scan is performed[30,33] also mean that direct comparisons of our texture results with those found in the literature must be made with care. Overall, the method of texture index (*T*)

*Assuming an $\varepsilon_{N=4}$ of 4.6 is imparted for a $\Phi = 90$ deg and $\Psi = 0$ deg die setup after $N = 4$ passes.[23]

**Toth *et al.* [57,59] stated that in order to obtain zero lattice spin ($\dot{\omega}$) for an ideal orientation, the plastic spin ($\dot{\beta}$) needs to negate the rigid body spin ($\dot{\Omega}$) since $\dot{\omega} = \dot{\Omega} - \dot{\beta}$. However, the value of $\dot{\beta}$ is large *only* when the number of operative slip systems is ≤2.

first suggested by Bunge *et al.*[24] should be used when quantifying *end*-texture strengths.

In the present results, the texture evolution leads to the following observations. After $N = 1$, monoclinic sample symmetry is lost as distinct nonuniformity and incompleteness in orientation density among the various fibers. Compared to other ECAE routes, processing *via* route B_C yields less fiberlike texture components, which can be segregated into f1, f2, and f3 fibers comprising $\{111\}_\theta$ and $<110>_\theta$ partials, respectively. This is in agreement with the equiaxed grain structure (after $N = 4$, 8, 12, and 16) observed by TEM and EBSD. Under conditions of *negative* SS, the end of each route B_C ECAE cycle (*i.e.*, every four passes) returns substantially weaker $A^*_{2\theta}$ and C_θ components in comparison to other ideal orientations. Such variations in the relative intensities of different texture components were also found with the changes in strain level in torsion experiments.[64,65] Increased strain accumulation during multipass ECAE also results in an increased spread of orientation density and a tendency of nonsymmetric orientation flow in the positive ϕ_1 direction[55] away from their ideal positions (in the sense of shear). This can be attributed to varying end-texture orientation stabilities after shear-type deformation. Again, such behavior has previously been noted by References 27, 33, and 45. After $N = 4$, 8, 12, and 16, the weak reappearance of texture components of the initial $N = 0$ pass sample reflect glide-reversal effects that return part of the substructure into an equiaxed configuration. This observation is also corroborated by the low ARs presented in Table I.

V. SUMMARY

Our results show that important information on the microstructural evolution of ECAE-processed Cu is gained if a combination of HR-EBSD, TEM, and XRD is used. The grain size measured by EBSD and TEM gradually decreases with increasing N, while the subgrain size remains approximately constant. The XRD peak broadening analyses indicate a smaller domain size than the subgrain size measured by TEM or EBSD, which can be attributed to faint dislocation networks present within cells and grains. In EBSD, the misorientation criterion used for the grains and subgrains indicates that, with increasing N, an increase in the volume fraction of HAGBs occurs up to 40 to 50 pct. More precisely, the increase of HAGBs is concentrated in the angular range between 35 and 60 deg, while the volume fraction of boundaries with intermediate (15 to 35 deg) angles remains roughly constant.

An assessment of the microstructural influence on the strengthening of the material has shown that a good match is obtained with the classical Hall–Petch relationship, if the subgrain size is taken as the dominating strengthening contribution, while the misorientation anglengle of s that the misorientation ening contribution.trengthening of the material has shown, thatallisation phenomena.ns can b h as is revealed to be of minor importance. This might be only valid for LAGBs of nonequilibrium, which due to the accumulation of dislocations contain a significantly higher number of excess dislocations than normal LAGBs.

Texture results indicate that under conditions of negative SS, route B_C processing results in less fiberlike development of orientation components along with a loss of monoclinic sample symmetry after the first pass. Increased accumulated strain through multiple ECAE passes results in a shift and spread of orientation components away from their ideal positions due to varying stabilities of end-texture orientations. Such differences in the strengths and characteristics of various ideal orientations are a product of the chosen processing route and also allude to the expected anisotropy in microstructural and mechanical properties.

ACKNOWLEDGMENTS

This work was performed under the auspices of the Monash University Engineering Research Committee Grant and ARC Discovery Project No. DP0557255. One of the authors (AAG) is in receipt of a Monash University International Postgraduate Research scholarship. The authors are grateful to Professor F.J. Humphreys, the Manchester Materials Science Centre (Manchester, United Kingdom), for permission to use the VMAP software package.

REFERENCES

1. F.J. Humphreys: *J. Mater. Sci.*, 2001, vol. 36 (16), pp. 3833–54.
2. J.R. Bowen, O.V. Mishin, P.B. Pragnell, and D.J. Jensen: *Scripta Mater.*, 2002, vol. 47 (5), pp. 289–94.
3. C.E. Krill and R. Birringer: *Phil. Mag. A*, 1998, vol. 77 (3), pp. 621–40.
4. C.P. Chang, P.L. Sun, and P.W. Kao: *Acta Mater.*, 2000, vol. 48 (13), pp. 3377–85.
5. O.V. Mishin, D.J. Jensen, and N. Hansen: *Mater. Sci. Eng. A*, 2003, vol. 342 (1–2), pp. 320–28.
6. F. Dalla Torre, P. Spätig, R. Schäublin, and M. Victoria: *Acta Mater.*, 2005, vol. 53 (8), pp. 2337–49.
7. T. Ungár: *Mater. Sci. Eng. A*, 2001, vols. 309–310, pp. 14–22.
8. D.A. Hughes and N. Hansen: *Acta Mater.*, 2000, vol. 48 (11), pp. 2985–3004.
9. T. Ungár, J. Gubicza, G. Ribárik, and A. Borbély: *J. Appl. Cryst.*, 2001, vol. 34 (3), pp. 298–310.
10. J. Gubicza, N.Q. Chinh, G. Krállics, I. Schiller, and T. Ungár: *Curr. Appl. Phys.*, 2006, vol. 6 (2), pp. 194–99.
11. M. Zehetbauer, E. Schafler, T. Ungár, I. Kopacz, and S. Bernstorff: *J. Eng. Mater. Technol.*, 2002, vol. 124, pp. 41–47.
12. N. Hansen: *Scripta Mater.*, 2004, vol. 51 (8), pp. 801–06.
13. E.O. Hall: *Proc. Phys. Soc., Ser. B*, 1951, vol. 64, pp. 747–53.
14. N.J. Petch: *J. Iron Steel Inst.*, 1953, vol. 174, pp. 25–28.
15. G.D. Hughes, S.D. Smith, C.S. Pande, H.R. Johnson, and R.W. Armstrong: *Scripta Mater.*, 1986, vol. 20, pp. 93–97.
16. A.M. El-Sherik, U. Erb, G. Palumbo, and K.T. Aust: *Scripta Metall. Mater.*, 1992, vol. 27, pp. 1185–88.
17. F.H. Dalla Torre, H. Van Swygenhoven, and M. Victoria: *Acta Mater.*, 2002, vol. 50 (15), pp. 3957–70.
18. V.Y. Gertsman, M. Hoffmann, H. Gleiter, and R. Birringer: *Acta Metall. Mater.*, 1994, vol. 42, pp. 3539–44.
19. R.Z. Valiev, N.A. Krasilnikov, and N.K. Tsenev: *Mater. Sci. Eng. A*, 1991, vol. 137 (1), pp. 35–40.
20. Y.J. Li, X.H. Zeng, and W. Blum: *Acta Mater.*, 2004, vol. 52 (17), pp. 5009–18.

21. V.M. Segal: *Mater. Sci. Eng. A*, 1995, vol. 197 (2), pp. 157–64.
22. F.H. Dalla Torre, R. Lapovok, J. Sandlin, P.F. Thomson, C.H.J. Davies, and E.V. Pereloma: *Acta Mater.*, 2004, vol. 52 (16), pp. 4819–32.
23. Y. Iwahashi, J. Wang, Z. Horita, M. Nemoto, and T.G. Langdon: *Scripta Mater.*, 1996, vol. 35 (2), pp. 143–46.
24. H.-J. Bunge: *Texture Analysis in Materials Science: Mathematical Methods*, 1st ed., P.R. Morris, ed., Butterworth & Co., Berlin, 1982.
25. D.G. Brandon: *Acta Metall.*, 1966, vol. 14, pp. 1479–1966.
26. G. Gottstein and L.S. Shvindlerman: *Applied Materials Science Technology*8, CRC Press, Boca Raton, FL, 1999, p. 408.
27. A.A. Gazder, F. Dalla Torre, C.F. Gu, C.H.J. Davies, and E.V. Pereloma: *Mater. Sci. Eng. A*, 2006, vol. 415 (1–2), pp. 126–39.
28. W.H. Huang, C.Y. Yu, P.W. Kao, and C.P. Chang: *Mater. Sci. Eng. A*, 2004, vol. 366 (2), pp. 221–28.
29. J. Gubicza, L. Balogh, R.J. Hellmig, Y. Estrin, and T. Ungár: *Mater. Sci. Eng. A*, 2005, vols. 400–401, pp. 334–38.
30. S. Li, I.J. Beyerlein, D.J. Alexander, and S.C. Vogel: *Scripta Mater.*, 2005, vol. 52 (11), pp. 1099–1104.
31. S. Li, I.J. Beyerlein, and M.A. Bourke: *Mater. Sci. Eng. A*, 2005, vol. 394 (1–2), pp. 66–77.
32. S. Li, I.J. Beyerlein, C.T. Necker, D.J. Alexander, and M.A. Bourke: *Acta Mater.*, 2004, vol. 52 (16), pp. 4859–75.
33. S. Li, I.J. Beyerlein, D.J. Alexander, and S.C. Vogel: *Acta Mater.*, 2005, vol. 53 (7), pp. 2111–25.
34. A. Vinogradov, T. Ishida, K. Kitagawa, and V.I. Kopylov: *Acta Mater.*, 2005, vol. 53 (8), pp. 2181–92.
35. A. Vinogradov, T. Suzuki, S. Hashimoto, K. Kitagawa, A. Kuznetsov, and S. Dobatkin: *Mater. Sci. Forum*, 2006, vols. 503–504, pp. 971–76.
36. Y. Iwahashi, Z. Horita, M. Nemoto, and T.G. Langdon: *Acta Mater.*, 1998, vol. 46 (9), pp. 3317–31.
37. S. Komura, Z. Horita, M. Nemoto, and T.G. Langdon: *J. Mater. Res.*, 1999, vol. 14 (10), pp. 4044–50.
38. M. Berta, P.J. Apps, and P.B. Prangnell: *Mater. Sci. Eng. A*, 2005, vols. 410–411, pp. 381–85.
39. A. Mishra, V. Richard, F. Grégori, R.J. Asaro, and M.A. Meyers: *Mater. Sci. Eng. A*, 2005, vols. 410–411, pp. 290–98.
40. Y.M. Wang, E. Ma, and M.W. Chen: *Appl. Phys. Lett.*, 2002, vol. 80 (13), pp. 2395–97.
41. S.C. Baik, R.J. Hellmig, Y. Estrin, and H.S. Kim: *Z. Metallkd.*, 2003, vol. 94, pp. 754–60.
42. B. Mingler, H.P. Karnthaler, M. Zehetbauer, and R.Z. Valiev: *Mater. Sci. Eng. A*, 2001, vols. 319–321, pp. 242–45.
43. Y. Iwahashi, Z. Horita, M. Nemoto, and T.G. Langdon: *Acta Mater.*, 1997, vol. 45 (11), pp. 4733–41.
44. J.R. Bowen: Ph.D. Thesis, University of Manchester Institute of Science and Technology, 2000, p. 301.
45. S. Li, A.A. Gazder, I.J. Beyerlein, C.H.J. Davies, and E.V. Pereloma: *Acta Mater.*, 2006, vol. 54 (4), pp. 1087–1100.
46. E. Nes: *Progr. Mater. Sci.*, 1997, vol. 41 (3), pp. 129–93.
47. O.V. Mishin, X. Huang, J.R. Brown, and D. Juul Jensen: *Proc. 22nd Risø Int. Symp. on Materials Science Recrystallization—Fundamental Aspects and Relations to Deformation Microstructure*, Roskilde, Denmark, 2001, pp. 335–40.
48. C.X. Huang, K. Wang, S.D. Wu, Z.F. Zhang, G.Y. Li, and S.X. Li: *Acta Mater.*, 2006, vol. 54 (3), pp. 655–65.
49. A.P. Sutton and R.W. Balluffi: *Interfaces in Crystalline Materials, Oxford Science Publications*, Clarendon Press, London, 1997, p. 852.
50. G. Wang, S.D. Wu, L. Zuo, C. Esling, Z.G. Wang, and G.Y. Li: *Mater. Sci. Eng. A*, 2003, vol. 346 (1–2), pp. 83–90.
51. C.F. Gu, F. Dalla Torre, J. Sandlin, E.V. Pereloma, and C.H.J. Davies: *Proc. 3rd Int. Conf. on Advanced Materials Processing*, IMEA Australasia Ltd, Melbourne, Australia, 2004.
52. R.Z. Valiev, V.Y. Gertsman, and O.A. Kaibyshev: *Phys. Status Solidi*, 1986, vol. 97, pp. 11–56.
53. S.R. Agnew and J.R. Weertman: *Mater. Sci. Eng. A*, 1998, vol. 242 (1–2), pp. 174–80.
54. A.A. Gazder, S. Li, F.H. Dalla Torre, I.J. Beyerlein, C.F. Gu, C.H.J. Davies, and E.V. Pereloma: *Mater. Sci. Eng. A*, 2006, vol. 437 (2), pp. 259–67.
55. J. Baczynski: Ph.D. Thesis, McGill University, Montreal, 1996, p. 208.
56. L.S. Tóth: *Proc. 2nd Int. Conf. on Nanomaterials by Severe Plastic Deformation: Fundamentals, Processing, Applications (Nano-SPD2)*, Materials Physics Institute, University of Vienna, Vienna, Austria, 2002.
57. L.S. Tóth: *Adv. Eng. Mater.*, 2003, vol. 5 (5), pp. 308–16.
58. L.S. Tóth, K.W. Neale, and J.J. Jonas: *Acta Metall.*, 1989, vol. 37 (8), pp. 2197–2210.
59. L.S. Tóth, P. Gilormini, and J.J. Jonas: *Acta Metall.*, 1988, vol. 36, pp. 3077–91.
60. S.C. Baik, Y. Estrin, R.J. Hellmig, H.T. Jeong, H.-G. Brokmeier, and H.S. Kim: *Z. Metallkd.*, 2003, vol. 94, p. 1189.
61. W.Q. Cao, A. Godfrey, W. Liu, and Q. Liu: *Mater. Sci. Eng. A*, 2003, vol. 360 (1–2), pp. 420–25.
62. S. Li, M.A.M. Bourke, I.J. Beyerlein, D.J. Alexander, and B. Clausen: *Mater. Sci. Eng. A*, 2004, vol. 382 (1–2), pp. 217–36.
63. S. Ferrasse, V.M. Segal, S.R. Kalidindi, and F. Alford: *Mater. Sci. Eng. A*, 2004, vol. 368 (1–2), pp. 28–40.
64. J. Baczynski and J.J. Jonas: *Acta Mater.*, 1996, vol. 44 (11), pp. 4273–88.
65. F. Montheillet, M. Cohen, and J.J. Jonas: *Acta Mater.*, 1984, vol. 32 (11), pp. 2077–89.